Journal of Sound and Vibration 344 (2015) 313–331

Contents lists available at ScienceDirect

Journal of Sound and Vibration

journal homepage: www.elsevier.com/locate/jsvi

Modal approach for nonlinear vibrations of damped impacted plates: Application to sound synthesis of gongs and cymbals

M. Ducceschi, C. Touzé *

Unité de Mécanique (UME), ENSTA-ParisTech, 828 Boulevard des Maréchaux, 91762 Palaiseau Cedex, France

ARTICLE INFO

Article history:
Received 10 September 2014
Received in revised form
8 January 2015
Accepted 21 January 2015
Handling Editor: W. Lacarbonara
Available online 16 February 2015

ABSTRACT

This paper presents a modal, time-domain scheme for the nonlinear vibrations of perfect and imperfect plates. The scheme can take into account a large number of degrees-of-freedom and is energy-conserving. The targeted application is the sound synthesis of cymbals and gong-like musical instruments, which are known for displaying a strongly nonlinear vibrating behaviour. This behaviour is typical of a wave turbulence regime, in which the wide-band spectrum of excited modes is observable in the form of an energy cascade. The modal method is selected for its versatility in handling complex damping laws that can be implemented easily by selecting appropriate damping values in each one of the modal equations. In the first part of the paper, the modal method is explained in its generality, and it will be seen that the method is valid for plates with arbitrary geometry and boundary conditions as long as the eigenmodes are known. Secondly, a time-integration, energy-conserving scheme for perfect and imperfect plates is presented, and implementation comments are given in order to treat efficiently the high-dimensionality of the resulting dynamical system. The scheme is run with appropriate parameters in order to produce sound samples. A simple impact law is considered for the excitation, whereas the flexibility of the method is highlighted by showing simulations for free-edge circular plates and simply-supported rectangular plates, together with various damping laws.

1. Introduction

Geometrically nonlinear vibrations of plates can exhibit a very rich and complex phenomenology when the vibration amplitude is larger than the thickness [1–3]. In a strongly nonlinear range, a wave turbulence regime can be excited with thousands of modes involved in an energy cascade from large to small wavelengths [4–7]. The energy cascade may be produced by shaking a large plate vigorously: this technique was used in the past in theaters to simulate the sound of thunders. Striking a large gong (in particular the Chinese tam-tam) results in a build-up of energy to the high-frequency range occurring a few milliseconds after the strike [8]: the bright, shimmering sound produced is another perceptual trace of the energy cascade [9,8,10] which is the phenomenon at the core of the wave turbulence theory.

The goal of the work presented here is the time-domain resolution of strongly nonlinear vibrations of plates, and the targeted application is the sound synthesis of gongs and cymbal-like instruments. The scheme is constructed in order to

* Corresponding author.
E-mail addresses: michele.ducceschi@ensta-paristech.fr (M. Ducceschi), cyril.touze@ensta-paristech.fr (C. Touzé).

http://dx.doi.org/10.1016/j.jsv.2015.01.029
0022-460X/

meet a number of salient features. Firstly, the numerical setup should be capable of simulating a complex damping mechanism, as loss effects are key in order to produce realistic sounds. Secondly, the scheme should be capable of calculating the linear (eigenfrequencies) as well as the nonlinear parameters with a high degree of accuracy. Finally, the method should be able to take into account thousands of modes interacting together in a strongly nonlinear regime.

From the numerical point of view, the dynamics is stiff and needs ad hoc time-stepping methods with robust stability. Within this field, finite difference methods have already been used with success, see e.g. [11,12,3]. However, temporal models for damping laws are difficult to implement in a finite-difference scheme, so that one usually resorts to a simplified loss model within this framework. Moreover, convergence of the eigenfrequencies and nonlinear terms is slow, so that, for increased accuracy, one needs to use very refined grids. A higher accuracy, in turn, is obtained at the expense of an increased computational burden that could quickly get out of reach. Another scheme has been developed in [13], based on a simplified shell model together with a modal approach and cubature schemes aimed at improving the computational time; despite being able to produce nonlinear sounds, such schemes do not produce a strongly nonlinear regime with an energy cascade, which – as it was pointed out – is the most desirable feature of gong and cymbals from an auditory perspective.

The aim of the present paper is to show that a modal method can be used to simulate efficiently the complex vibratory response of vibrating plates at large amplitudes. One advantage of the proposed method relies in the fact that modal damping can be tuned at will to fit specific damping laws (obtained from measurements or otherwise). As the perception of losses is key in order to retrieve realistic sounds, this feature is essential in the choice of the method. The equations to be solved are the von Kármán equations for plates. The numerical challenge in this context resides in the very large number of modes involved in the vibrations. A key point in the proposed method is to use a conservative scheme for the time integration, where stability is obtained as a direct consequence of energy conservation.

The paper is organized as follows. In Section 2, the von Kármán plate model is recalled. Then the modal approach is developed in a general framework, without referring to a particular geometry, nor to specific boundary conditions. It is only assumed that the eigenproblem has been solved and that the modes are known in some manner (by analytic or numerical methods). The conservative scheme for the resulting set of Ordinary Differential Equations (ODEs) is then given, and it is shown that discrete numerical energy is conserved. Section 3 shows how the method can be applied to synthesize the sound of gongs and cymbals. The cases of two plates with different geometries and boundary conditions are proposed as illustrative examples. The first of such cases is that of a circular plate with a free edge, for which the modes are analytic. The second case is that of a rectangular plate with simply supported, in-plane movable edges: this is a more difficult case because the in-plane modes do not have an analytic solution and thus a numerical strategy is required. The versatility of the method is illustrated by synthesizing realistic sounds of gongs and cymbal-like instruments. The method, being completely general, can be extended to any other type of boundary conditions and geometry for plates whose nonlinear dynamics is described by the von Kármán equations. Thanks to this method – with reasonable computational resources – simulations of strongly nonlinear regimes with up to a thousand interacting modes are possible. It is hoped that this result will give new impetus to modal methods for time-domain simulations in nonlinear regimes.

2. Models and methods

2.1. The von Kármán equations for perfect plates

The model equations for strongly nonlinear vibrations of plates considered in this paper are the von Kármán [14–17]. The basic assumptions for such system can be found in many textbooks and articles, see e.g. [17–19], and they are briefly recalled here: the material of the plate is supposed to behave according to the linear elasticity theory; the kinematics is of Kirchoff–Love type and thus transverse shear is neglected; the in-plane Green–Lagrange strain tensor is truncated so to keep a single second-order correction to the linear part. When in-plane external forcing is not present, an Airy stress function can be used in order to describe longitudinal motions. The equations of motion are then expressed in terms of the transverse displacement $w(\mathbf{x},t)$ and the Airy stress function $F(\mathbf{x},t)$, where $\mathbf{x}$ denotes the (two-dimensional) space variable and t the time, and are often referred to as the Föppl–von Kármán equations [18]. They read for perfect isotropic plates:

$$\rho h\ddot{w}+D\Delta\Delta w=\mathcal{L}(w,F)+p(\mathbf{x},t)-R(\dot{w}), \tag{1a}$$

$$\Delta\Delta F=-\frac{Eh}{2}\mathcal{L}(w,w), \tag{1b}$$

where ρ is the material volume density, h the plate thickness, and D stands for flexural rigidity: $D=Eh^3/12(1-\nu^2)$, with E and ν respectively Young modulus and Poisson ratio. Δ represents the two-dimensional Laplacian operator, while $p(\mathbf{x},t)$ stands for the normal external forcing, and $R(\dot{w})$ is a generic expression for the viscous damping depending on the velocity field. Both p and R functions will be given when needed. The operator $\mathcal{L}$ is generally referred to as the "von Kármán operator" or "Monge–Ampère form" in the literature [17,20] and may be expressed in intrinsic coordinates, for two functions $f(\mathbf{x})$ and $g(\mathbf{x})$, as

$$\mathcal{L}(f,g)=\Delta f\Delta g-\nabla\nabla f:\nabla\nabla g, \tag{2}$$

where : denotes the doubly contracted product of two tensors.

2.2. Modal approach

In this section the main steps of the discretization, using the linear normal modes as basis functions in the Galerkin procedure, are briefly recalled. The derivation is provided in a general manner, hence no specific boundary conditions are given and the explicit form of the eigenfunctions are not stated. It is only assumed that the linear problem is solved by a given method, analytical or numerical. Let $\{\Phi_k(\mathbf{x})\}_{k\geq 1}$ be the eigenmodes of the transverse displacement. These functions are the solutions of the Sturm–Liouville eigenvalue problem:

$$\Delta\Delta\Phi_k(\mathbf{x}) = \frac{\rho h}{D}\omega_k^2\Phi_k(\mathbf{x}), \tag{3}$$

together with the associated boundary conditions. In Eq. (3), ω_k stands for the kth radian eigenfrequency. The linear modes are defined up to a constant of normalization that can be chosen arbitrarily. For the sake of generality, S_w denotes the constant of normalization of the function $\overline{\Phi} = S_w\Phi_k(\mathbf{x})/\|\Phi_k\|$. The norm is obtained from a scalar product $\langle\alpha,\beta\rangle$ between two functions $\alpha(\mathbf{x})$ and $\beta(\mathbf{x})$, defined as

$$\langle\alpha,\beta\rangle = \int_S \alpha\,\beta\,\mathrm{d}S \longrightarrow \|\Phi_k\|^2 = \langle\Phi_k,\Phi_k\rangle, \tag{4}$$

where S represents the area of the plate. The eigenmodes for the Airy stress function are also considered and denoted as $\{\Psi_k(\mathbf{x})\}_{k\geq 1}$. They are solutions of the following eigenvalue problem:

$$\Delta\Delta\Psi_k(\mathbf{x}) = \zeta_k^4\Psi_k(\mathbf{x}), \tag{5}$$

together with the associated boundary conditions for F. The linear modes so defined are orthogonal with respect to the scalar product, and are therefore a suitable function basis [21]. Orthogonality between two functions $\Lambda_m(x,y),\Lambda_n(x,y)$ is expressed as

$$\langle\Lambda_m,\Lambda_n\rangle = \delta_{m,n}\|\Lambda_m\|^2, \tag{6}$$

where $\delta_{m,n}$ is Kronecker's delta.

The Partial Differential equations (1) for the perfect plate are discretized by expanding the two unknowns w and F along their respective eigenmodes

$$w(\mathbf{x},t) = S_w\sum_{k=1}^{N_\Phi}\frac{\Phi_k(\mathbf{x})}{\|\Phi_k\|}q_k(t), \tag{7a}$$

$$F(\mathbf{x},t) = S_F\sum_{k=1}^{N_\Psi}\frac{\Psi_k(\mathbf{x})}{\|\Psi_k\|}\eta_k(t), \tag{7b}$$

where $q_k(t)$ and $\eta_k(t)$ represent respectively the modal transverse displacement and the modal coordinate for the Airy stress function. The integers N_Φ and N_Ψ represent respectively the number of transverse and in-plane modes that will be kept in the truncations to ensure convergence. Using a standard Galerkin procedure, Eqs. (7) are first introduced in Eq. (1b), which is then multiplied by Ψ_k. Integrating over the surface of the plate and using the orthogonality relationship one obtains

$$\eta_k = -\frac{Eh}{2\zeta_k^4}\frac{S_w^2}{S_F}\sum_{i,j}^{N_\Phi}q_iq_j\frac{\int_S\Psi_k\mathcal{L}(\Phi_i,\Phi_j)\,\mathrm{d}S}{\|\Psi_k\|\,\|\Phi_i\|\,\|\Phi_j\|}. \tag{8}$$

The coefficient appearing in Eq. (8) can be rewritten as

$$H_{i,j}^k = \frac{\int_S\Psi_k\mathcal{L}(\Phi_i,\Phi_j)\,\mathrm{d}S}{\|\Psi_k\|\,\|\Phi_i\|\,\|\Phi_j\|}, \tag{9}$$

and expresses the nonlinear coupling between in-plane and transverse motions. Following the same procedure, Eqs. (7) are introduced in Eq. (1a). Multiplying by Φ_s and integrating over the surface leads to

$$\ddot{q}_s + \omega_s^2q_s + 2\xi_s\omega_s\dot{q}_s = \frac{S_F}{\rho h}\sum_{i=1}^{N_\Phi}\sum_{j=1}^{N_\Psi}q_i\eta_j\frac{\int_S\Phi_s\mathcal{L}(\Phi_i,\Psi_j)\,\mathrm{d}S}{\|\Phi_s\|\,\|\Phi_i\|\,\|\Psi_j\|} + p_s(t). \tag{10}$$

The coefficient appearing in Eq. (10) is rewritten as

$$E_{i,j}^s = \frac{\int_S\Phi_s\mathcal{L}(\Phi_i,\Psi_j)\,\mathrm{d}S}{\|\Phi_s\|\,\|\Phi_i\|\,\|\Psi_j\|}. \tag{11}$$

Note that in Eq. (10), the modal external force has been expressed as

$$p_s(t) = \frac{1}{\rho h S_w\|\Phi_s\|}\int_S p(\mathbf{x},t)\Phi_s(\mathbf{x})\,\mathrm{d}S. \tag{12}$$

Note also that a modal damping term has been introduced as $2\xi_s\omega_s\dot{q}_s$ in Eq. (10). This modal damping ratio can be tuned at

will by selecting appropriate values for each ξ_s. Such values may be derived from experiments, see e.g. [22,23], and thus they will be used in the remainder of this paper for describing losses in the system.

Grouping together Eqs. (10) and (8) gives the temporal system of Ordinary Differential Equations (ODEs) to solve as

$$\ddot{q}_s+\omega_s^2 q_s+2\xi_s\omega_s\dot{q}_s=\frac{S_F}{\rho h}\sum_{k=1}^{N_\Phi}\sum_{l=1}^{N_\Psi}E^s_{k,l}q_k\eta_l+p_s(t), \tag{13a}$$

$$\eta_l=-\frac{Eh}{2\zeta_l^4}\frac{S_w^2}{S_F}\sum_{m,n}^{N_\Phi}H^l_{m,n}q_mq_n. \tag{13b}$$

Elimination of the auxiliary variable η_l from Eqs. (13) is generally performed (see e.g. [24–26,15,2]) by substituting (13b) in (13a), resulting in a closed system for the transverse modal displacements

$$\ddot{q}_s+\omega_s^2 q_s+2\xi_s\omega_s\dot{q}_s=-\frac{ES_w^2}{\rho}\sum_{k,m,n}^{N_\Phi}\left[\sum_{l=1}^{N_\Psi}\frac{H^l_{m,n}E^s_{k,l}}{2\zeta_l^4}\right]q_kq_mq_n+p_s(t), \tag{14}$$

where the fourth-order tensor $\Gamma^s_{k,m,n}$ may be introduced [17,27] as

$$\Gamma^s_{k,m,n}=\sum_{l=1}^{N_\Psi}\frac{H^l_{m,n}E^s_{k,l}}{2\zeta_l^4}. \tag{15}$$

In the present study, both the quadratic and cubic formulations will be used: the quadratic (q,η) formulation expressed in Eqs. (13) will be the basis for the numerical scheme shown in Section 2.5; however, in order to assess the accuracy of the scheme, convergence of a few values of the cubic coupling coefficients $\Gamma^s_{k,m,n}$ appearing in will be discussed in some detail in later sections.

2.3. Symmetry properties

This section is intended to recall some important symmetry properties of the presented tensors $(H^k_{i,j},E^l_{m,n})$. These properties will be of some importance in the remainder of the paper, as they enable the derivation of the stable conservative scheme. Moreover, the same properties can be employed in order to reduce the memory and computational burden of the scheme.

The first obvious symmetry is for $H^k_{i,j}$, and states that

$$H^k_{i,j}=H^k_{j,i}, \tag{16}$$

as a direct consequence of the bilinear symmetry of the von Kármán operator $\mathcal{L}(\cdot,\cdot)$.

The second property links $H^k_{i,j}$ and $E^l_{m,n}$ using the so-called triple self-adjointness property (TSA) of the von Kármán operator $\mathcal{L}(\cdot,\cdot)$, fully studied in [17,28]. The TSA stems from the following identity, for three given functions f,g,h,

$$\int_S f\mathcal{L}(g,h)\,\mathrm{d}S=\int_S\mathcal{L}(f,g)h\,\mathrm{d}S+\mathcal{C}, \tag{17}$$

where $\mathcal{C}$ is a contour integral, the complete expression of which may be found in [17]. In most cases, this contour integral $\mathcal{C}$ vanishes, giving rise to a straightforward relationship between the coefficients as

$$E^l_{m,n}=H^n_{m,l}. \tag{18}$$

An exhaustive list where the contour integral vanishes, depending on the classical boundary conditions, is given in [17]. Note that this property is assumed to be fulfilled in the remainder of the paper; as a consequence, the conservative scheme presented after cannot be applied to the cases for which (18) does not hold.

2.4. Continuous and discrete modal energies

In this section, the kinetic and potential energies for the von Kármán thin plate equations are recalled, as they are needed for identification when deriving the conservative scheme. The continuous expressions of the energies can be found in [15,29,3,28] and read

$$T=\int_S\frac{\rho h}{2}\dot{w}^2\,\mathrm{d}S, \tag{19a}$$

$$V=\int_S\frac{D}{2}(\Delta w)^2\,\mathrm{d}S, \tag{19b}$$

$$U=\int_S\frac{1}{2Eh}(\Delta F)^2\,\mathrm{d}S, \tag{19c}$$

for, respectively, the kinetic energy T, the flexural stored energy V and the membrane energy U. Note that the in-plane energy term U has been here expressed with respect to the Airy stress function F.

The modal counterparts of the energies are derived by introducing the modal expansions (7) and using the properties of the eigenmodes together with integration by parts. One finally gets

$$T = \frac{\rho h}{2} S_w^2 \sum_{k=1}^{N_\Phi} \dot{q}_k^2(t), \tag{20a}$$

$$V = \frac{\rho h}{2} S_w^2 \sum_{k=1}^{N_\Phi} \omega_k^2 q_k^2(t), \tag{20b}$$

$$U = \frac{S_F^2}{2Eh} \sum_{k=1}^{N_\Psi} \zeta_k^4 \eta_k^2(t). \tag{20c}$$

When damping and forcing are not considered, the total energy $E = T+V+U$ is conserved, and reads

$$\frac{\mathrm{d}}{\mathrm{d}t}(T+V+U) = 0. \tag{21}$$

2.5. Energy-conserving scheme

In this section, a stable scheme for the perfect plate is presented. This scheme is taken from [29], where a full finite-difference method for the von Kármán equations is presented. The temporal part of such scheme is here applied to the modal equations. The conservation of energy for the modal equations and its specific arguments are here presented for the first time. The scheme is applicable for the undamped and unforced perfect plate in the modal description given by Eqs. (13), i.e. in the quadratic (q,η) formulation. Let us first introduce a list of discrete time operators acting on a state vector $\mathbf{q}(n)$ defined at time step n. The backward and forward shift operators are, respectively,

$$e_{t-}\mathbf{q}(n) = \mathbf{q}(n-1); \quad e_{t+}\mathbf{q}(n) = \mathbf{q}(n+1). \tag{22}$$

Backward, centered, forward approximations to first time derivatives are defined as

$$\delta_{t-} \equiv \frac{1}{k}(1-e_{t-}); \quad \delta_{t\cdot} \equiv \frac{1}{2k}(e_{t+}-e_{t-}); \quad \delta_{t+} \equiv \frac{1}{k}(e_{t+}-1), \tag{23}$$

where $k = 1/f_S$ refers to the timestep, f_S being the sampling frequency. An approximation to the second time derivative can be constructed by combining the previous operators,

$$\delta_{tt} \equiv \delta_{t+}\delta_{t-} = \frac{1}{k^2}(e_{t+}-2+e_{t-}). \tag{24}$$

Backward, centered, forward averaging operators are introduced as

$$\mu_{t-} \equiv \frac{1}{2}(1+e_{t-}); \quad \mu_{t\cdot} \equiv \frac{1}{2}(e_{t+}+e_{t-}); \quad \mu_{t+} \equiv \frac{1}{2}(e_{t+}+1). \tag{25}$$

The temporal conservative scheme for the case of the perfect, undamped and unforced plate reads

$$\delta_{tt} q_s(n) + \omega_s^2 q_s(n) = \frac{S_F}{\rho h} \sum_{k=1}^{N_\Phi} \sum_{l=1}^{N_\Psi} E_{k,l}^s q_k(n) \left[\mu_{t\cdot}\eta_l(n)\right]; \tag{26a}$$

$$\mu_{t-}\eta_l(n) = -\frac{Eh}{2\zeta_l^4}\frac{S_w^2}{S_F} \sum_{i,j=1}^{N_\Phi} H_{i,j}^l q_i(n) \left[e_{t-} q_j(n)\right]. \tag{26b}$$

This scheme is second-order accurate and implicit: due to the presence of the centered averaging operator in Eq. (26a), the coefficient multiplying the vector $\mathbf{q}(n+1)$ depends on the timestep.

Let us now demonstrate that the proposed scheme is energy-conserving. The idea is to retrieve a counterpart of Eq. (21) at the discrete level. To that purpose, Eq. (26a) is multiplied by $\rho h \delta_{t\cdot} q_s(n)$ and then summed over the index s. In addition, Eq. (26b) is multiplied by δ_{t+}, so that

$$\rho h \sum_{s=1}^{N_\Phi} (\delta_{t\cdot} q_s(n)) \delta_{tt}\, q_s(n) + \rho h \sum_{s=1}^{N_\Phi} (\delta_{t\cdot} q_s(n)) \omega_s^2 q_s(n) = S_F \sum_{k,s=1}^{N_\Phi} \sum_{l=1}^{N_\Psi} E_{k,l}^s (\delta_{t\cdot} q_s(n)) q_k(n) (\mu_{t\cdot}\, \eta_l(n)) \tag{27a}$$

$$\mu_{t-}(\delta_{t+}\eta_l(n)) = -\frac{EhS_w^2}{2\zeta_l^4 S_F} \sum_{k,s=1}^{N_\Phi} \frac{1}{k} H_{k,s}^l (q_k(n+1)q_s(n) - q_k(n)q_s(n-1)) \tag{27b}$$

Now, owing to the symmetry property of the H tensor, see Eq. (16), the indices of the first term on the right-hand side of Eq. (27b) can be swapped to give

$$\frac{1}{k}H^l_{k,s}\left(q_k(n+1)q_s(n)-q_k(n)q_s(n-1)\right)=2H^l_{k,s}q_k(n)\delta_{t\cdot}q_s(n) \tag{28}$$

Hence, Eq. (27b) can be rewritten as

$$-\frac{\zeta_l^4 S_F}{EhS_w^2}\mu_{t-}\left(\delta_{t+}\eta_l(n)\right)=\sum_{k,s=1}^{N_\Phi}H^l_{k,s}q_k(n)\delta_{t\cdot}q_s(n) \tag{29}$$

Owing to the triple self-adjointness property, one may use Eq. (18) stating that $E^s_{k,l}=H^l_{k,s}$, and insert the left-hand side of Eq. (29) into the right-hand side of Eq. (27a), yielding

$$S_F\sum_{k,s=1}^{N_\Phi}\sum_{l=1}^{N_\Psi}H^l_{k,s}\left(\delta_{t\cdot}q_s(n)\right)q_k(n)\left(\mu_{t\cdot}\eta_l(n)\right)=-\frac{S_F^2}{EhS_w^2}\sum_{l=1}^{N_\Psi}\zeta_l^4\left[\mu_{t-}\left(\delta_{t+}\eta_l(n)\right)\right]\left(\mu_{t\cdot}\eta_l(n)\right),=-\frac{S_F^2}{2EhS_w^2}\delta_{t+}\sum_{l=1}^{N_\Psi}\zeta_l^4\mu_{t-}\left(\eta_l(n)^2\right). \tag{30}$$

The left-hand side of Eq. (27a) can be rewritten as

$$\rho h\sum_{s=1}^{N_\Phi}\left(\delta_{t\cdot}q_s(n)\right)\delta_{tt}\,q_s(n)+\rho h\sum_{s=1}^{N_\Phi}\left(\delta_{t\cdot}q_s(n)\right)\omega_s^2q_s(n)=\frac{\rho h}{2}\delta_{t+}\sum_{s=1}^{N_\Phi}\left(\left(\delta_{t-}q_s(n)\right)^2+\omega_s^2q_s(n)\left(e_{t-}q_s(n)\right)\right) \tag{31}$$

Putting together Eqs. (30) and (31) gives

$$\delta_{t+}\left\{\sum_{s=1}^{N_\Phi}S_w^2\frac{\rho h}{2}\left[\left(\delta_{t-}q_s(n)\right)^2+\omega_s^2q_s(n)\left(e_{t-}q_s(n)\right)\right]+\frac{S_F^2}{2Eh}\sum_{l=1}^{N_\Psi}\zeta_l^4\left(\mu_{t-}\left(\eta_l(n)\eta_l(n)\right)\right)\right\}=0. \tag{32}$$

The discrete counterparts of kinetic and potential energies defined by Eqs. (19) can now be identified from Eq. (32) as

$$\mathfrak{t}=\sum_{m=1}^{N_\Phi}\tau_m(n)=\frac{\rho h}{2}S_w^2\sum_{m=1}^{N_\Phi}\left(\delta_{t-}q_m(n)\right)^2, \tag{33a}$$

$$\mathfrak{v}=\sum_{m=1}^{N_\Phi}\nu_m(n)=\frac{\rho h}{2}S_w^2\sum_{m=1}^{N_\Phi}\omega_m^2q_m(n)\left(e_{t-}q_m(n)\right), \tag{33b}$$

$$\mathfrak{u}=\sum_{l=1}^{N_\Psi}\upsilon_l(n)=\frac{S_F^2}{2Eh}\sum_{l=1}^{N_\Psi}\zeta_l^4\left(\mu_{t-}\left(\eta_l(n)\eta_l(n)\right)\right), \tag{33c}$$

where the modal contributions to kinetic and potential energies, $\tau_m(n)$, $\nu_m(n)$ and $\upsilon_l(n)$ have also been introduced. With these notations, Eq. (32) is a discrete counterpart to Eq. (21), as it reads $\delta_{t+}(\mathfrak{t}+\mathfrak{v}+\mathfrak{u})=0$.

To conclude the proof, let us show that the discrete energy is positive definite. The in-plane discrete potential energy $\mathfrak{u}$ is positive definite, being the sum of squared numbers. Let us now consider the remaining term, $\epsilon^l_m(n)=\tau_m(n)+\nu_m(n)$, which is the contribution to the linear energy of the transverse mode m at the time n. Developing the operators in the definition of $\epsilon^l_m(n)$ gives

$$\epsilon^l_m(n)=\frac{\rho h}{2}S_w^2\left(\frac{q_m(n)q_m(n)+q_m(n-1)q_m(n-1)-2q_m(n)q_m(n-1)}{k^2}+\omega_m^2\,q_m(n)q_m(n-1)\right). \tag{34}$$

This last expression can be written as the equation of a conic in the $x-y$ space, where $x=q_m(n)$ and $y=q_m(n-1)$. This gives

$$x^2+y^2+2\alpha xy=\frac{2k^2\epsilon^l_m(n)}{\rho hS_w^2}\quad\text{with }\alpha=\frac{k^2\omega_m^2}{2}-1. \tag{35}$$

A closed conic (ellipse or circle) is obtained when $|\alpha|<1$, in which case one obtains the two following relationships:

$$\frac{2k^2\epsilon^l_m(n)}{\rho hS_w^2}>0 \tag{36}$$

$$|x|,|y|\le\sqrt{\frac{2k^2\epsilon^l_m(n)}{\rho h(1-\alpha^2)S_w^2}}. \tag{37}$$

Eq. (36) shows that $\epsilon^l_m(n)>0$, so that the discrete energies introduced are positive definite. Eq. (37) is the bound on the solution size. Note that the stability condition $|\alpha|<1$ is obtained when

$$k<\frac{2}{\omega_m}, \tag{38}$$

which gives the bound on the step size k for ensuring stability. This relationship must be fulfilled for all $m=1,\ldots N_\Phi$; thus

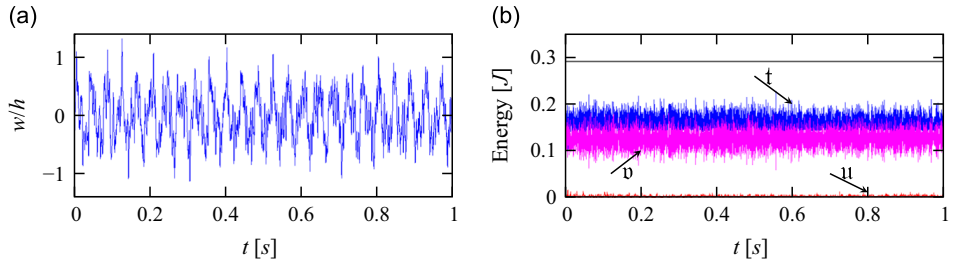

Fig. 1. Numerical demonstration of energy conservation. Rectangular undamped plate of lateral dimensions L_x=0.4 m, L_y=0.6 m, thickness h=1 mm, excited by a Dirac delta function of amplitude 1000 N (duration of one sample). (a) Displacement of the plate at $\mathbf{x}_0 = [0.51L_x\ 0.11L_y]$, normalized by the thickness. (b) Energies. The black continuous and constant thin line is the total discrete energy $\mathfrak{h} = \mathfrak{t} + v + u$. Blue thin line (black in BW printing): kinetic energy $\mathfrak{t}$, magenta thin oscillating line (grey in BW printing) : flexural stored energy $\mathfrak{v}$. The red thin line oscillating near 0 is the membrane (in-plane) energy $\mathfrak{u}$. (For interpretation of the references to color in this figure caption, the reader is referred to the web version of this paper.)

the most restrictive case is obtained when $m = N_\Phi$. Hence the associated sampling rate $f_S = 1/k$ is directly related to the largest eigenfrequency retained in the truncation: $f_{N_\Phi} = \omega_{N_\Phi}/2\pi$, through the simple relationship: $f_S > \pi f_{N_\Phi}$. In practice, for a given modal truncation at N_Φ the minimum step size is immediately calculated. The associated sampling frequency appears to be small, as only 3 points per period discretize the highest frequency of the system. This is another appealing property of the energy-conserving scheme. Note finally that the conservative scheme has been introduced here for the case of perfect plates. The scheme is extended to the case of the von Kármán plate equations with a static, geometric imperfection, in Appendix A.

The conservation of energy is shown on a particular example and illustrated in Fig. 1. A rectangular plate of lateral dimensions L_x=0.4 m, L_y=0.6 m, thickness h=1 mm, and made of steel with material parameters E=200 GPa, ν=0.3 and density ρ=7860 kg m^{-3} is selected. The boundary conditions are simply supported for the transverse motions and free for the in-plane motions. This particular case will be used again in Section 3.3 where more details will be given on the computational framework for the eigenmodes. For this illustrative example, the plate is undamped and excited by a Dirac delta function in space and time, located at excitation point $\mathbf{x}_{in} = [0.45L_x\ 0.45L_y]$, and with an amplitude of 1000 N. The number of transverse modes retained for the simulation is N_Φ=100, and N_Ψ=200 for the in-plane modes. The eigenfrequency of the 100th transverse mode is 1400 Hz, and the minimum sampling rate according to Eq. (38) is 4400 Hz. The sampling frequency has been selected as f_S=10 000 Hz for the simulation. With that set-up, computation of the H coefficients lasts 16 s while computing one second of simulation lasts 55 s. Fig. 1(a) shows the output displacement at point $\mathbf{x}_0 = [0.51L_x\ 0.11L_y]$, which is of the order of the thickness h so that geometric nonlinearities are excited. Fig. 1(b) shows the three components $\mathfrak{t}$, $\mathfrak{v}$, $\mathfrak{u}$ of the energy and the sum is found to be perfectly conserved up to machine accuracy.

2.6. Note on implementation details

Now that the theoretical aspects of the modal approach have been presented, it is worth outlining a brief discussion regarding practical implementation details. As a rule of thumb, one should implement the modal code in two parts, the first being the offline calculation of the eigenmodes and coupling coefficients, and the second being the actual time integration. It is worth stressing the fact that circular plates and rectangular plates of the same aspect ratio have the same eigenmodes and coupling coefficients (up to a multiplicative constant) and so the offline calculation can be done once and for all for a whole family of plates.

A second observation considers the memory requirements for the fourth-order coefficient tensor $\Gamma^s_{n,p,q}$. Because the simulations comprise usually a large number of modes (say, $N_\Phi \sim 500$), the physical memory occupied by the tensor is enormous (for 500^4 double precision entries, this is of the order of 500 Gb). This problem can be circumvented in two ways:

- by making use of the symmetry properties detailed in Section 2.3, which yield families of indices (s,n,p,q) which correspond to the same numerical value. This value can be calculated once and applied to the whole family;
- by storing the sole tensor $H^k_{i,j}$ of considerable smaller size.

The latter choice is particularly useful for memory savings: with $N_\Phi = 500$, $N_\Psi = 200$, a double-precision tensor file occupies about 0.4 Gb of physical memory. Note that, when using a numerical computing environment such as Matlab, nested loops should be avoided at all times, and replaced by convenient tensor multiplications. Matlab implementation of the modal code is possible and yields reasonable calculation times, as a few examples in the next section will demonstrate. In particular, products appearing on e.g. the right-hand sides of Eqs. (26a) and (26b) can be vectorized with proper matrix representations, so that no loops are needed to compute them, see [28] for more details.

3. Applications to sound synthesis of cymbal and gong-like instruments

This section is concerned with application of the conservative modal scheme to the case of damped impacted plates, with the purpose of synthesizing the sound of gongs and cymbal-like instruments. The performance of the method will be highlighted by demonstrating its ability in producing strongly nonlinear dynamics with a large number of modes involved in a regime of wave turbulence. Two different cases will be shown: a circular plate with a free edge, and a rectangular plate with simply supported and in-plane movable edges. First, the excitation force used for both simulation set-ups is briefly explained.

3.1. Excitation

The excitation is assumed to represent the case of an impact (such that of a mallet in the case of the gong or a drumstick in the case of a cymbal) on a given point $\mathbf{x}_0$ on the surface of the plate. In the simplest case, the force model is in the form of a pointwise contact

$$p(\mathbf{x},t)=\delta(\mathbf{x}-\mathbf{x}_0)g(t) \tag{39}$$

together with a temporal distribution having the form of a raised cosine [11]:

$$g(t)=\begin{cases}\dfrac{p_m}{2}\left[1+\cos\left(\pi(t-t_0)/T_{wid}\right)\right] & \text{if } |t-t_0|\le T_{wid};\\ 0 & \text{if } |t-t_0|>T_{wid}.\end{cases} \tag{40}$$

The temporal distribution is represented in Fig. 2. Two input parameters can be selected so as to mimic the force interaction produced by the impact of a drumstick (hard impact with a short time interaction of the order of 1 ms) or a mallet (soft impact with a longer time interaction of the order of 5–10 ms): half the interaction time T_{wid}, and the maximum of the force amplitude p_m. Fig. 2 shows two different examples for a rather soft impact ($T_{wid}=5$ ms, $p_m=20$ N), and a hard one ($T_{wid}=1$ ms, $p_m=100$ N).

3.2. A circular plate with a free edge

3.2.1. Geometry and boundary conditions

A circular plate of radius a and thickness h, with a free edge, is first considered. The boundary conditions then read, for the two unknowns $w(r,\theta,t)$ and $F(r,\theta,t)$ [25]:

$$\forall t,\ \forall\theta\in[0,2\pi],\quad w_{,rr}+\frac{\nu}{a}w_{,r}+\frac{\nu}{a^2}w_{,\theta\theta}=0\quad \text{at } r=a, \tag{41a}$$

$$w_{,rrr}+\frac{1}{a}w_{,rr}-\frac{1}{a^2}w_{,r}+\frac{2-\nu}{a^2}w_{,r\theta\theta}-\frac{3-\nu}{a^3}w_{,\theta\theta}=0\quad \text{at } r=a, \tag{41b}$$

$$F_{,r}+\frac{1}{a}F_{,\theta\theta}=0,\quad F_{,r\theta}+\frac{1}{a}F_{,\theta}=0\quad \text{at } r=a. \tag{41c}$$

Besides the advantage of simulating a geometry which is close to that of a gong or a cymbal, there are two mathematical advantages of the circular geometry with a free edge. First the eigenmodes for both the transverse displacement and the Airy stress function are analytic, and can thus be easily tabulated in order to compute the nonlinear coupling coefficients $H^p_{i,j}$. The eigenfunctions are combinations of Bessel functions. They are given in [25], and recalled in Appendix B for the sake of completeness. The eigenfunctions are here denoted by either a single integer number p – sorting the frequencies from small to large – or by a pair (k,n), where k denotes the number of nodal diameters and n the number of nodal circles. As it is usual with circular symmetry, asymmetric modes with $k\neq 0$ are degenerated so that two eigenvectors are found for the same

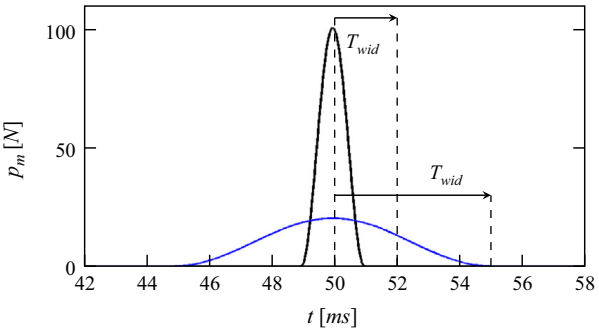

Fig. 2. Impact force model used for the simulations, centered at $t_0=50$ ms. Blue line: soft impact with $T_{wid}=5$ ms, $p_m=20$ N. Black line: hard impact with $T_{wid}=1$ ms and $p_m=100$ N. (For interpretation of the references to color in this figure caption, the reader is referred to the web version of this paper.)

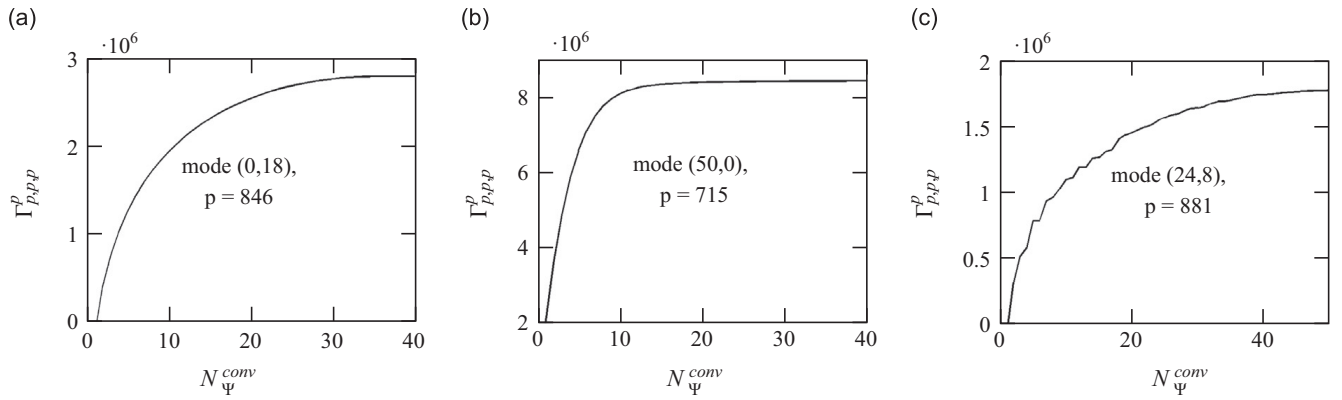

Fig. 3. Convergence of nondimensional coupling coefficient $\Gamma^p_{p,p,p}$ as a function of the number of in-plane admissible modes N_Ψ^{conv}, for (a) $p=846$, axisymmetric mode (0,18); (b) $p=715$, mode (50,0); (c) $p=881$, mode (24,8).

Table 1
Nondimensional values of eigenfrequencies ω_{kn} and coupling coefficients $\Gamma^p_{p,p,p}$ for some modes of the circular plate with a free edge. The modes are sorted with respect to increasing eigenfrequencies.

Mode label p	Mode (k,n)	ω_{kn}	$\omega_{kn}/\omega_{(2,0)}$	$\Gamma^p_{p,p,p}$	N_Ψ^{conv}
1,2	(2,0)	5.093	1	1.898	3
3	(0,1)	9.175	1.8	8.575	4
4,5	(3,0)	11.90	2.3	17.03	4
715,716	(50,0)	2687.9	527.7	8.436×10^6	65
846	(0,18)	3196.8	627.6	2.846×10^6	36
881,882	(24,8)	3352.1	658.1	1.783×10^6	50

eigenfrequency. The second advantage is that the von Kármán equations can be made nondimensional with respect to the radius a and thickness h, following e.g. [25]. Hence all the data for the model (eigenfrequencies, coupling coefficients) can be computed once and for all, since changing the radius or the thickness does not change the nondimensional equations. This case is very different from that of a rectangular plate for instance, where the aspect ratio between the lengths is a parameter that appears in the nondimensional equations. One can take advantage of these two specific features in order to greatly simplify the implementation details and speed up the calculations.

3.2.2. *Coupling coefficients*

For the circular plate, eigenfrequencies for both the transverse and in-plane problems are analytic so that the numerical values of $\{\omega_k,\ \zeta_p\}_{k,p\geq 1}$ used to feed the model can be considered exact. In the truncation process, the number of in-plane modes N_Ψ should be evaluated by looking at the convergence of the cubic coupling coefficient $\Gamma^p_{p,p,p}$ defined in Eq. (15), see e.g. [25,27,30]. As explained in [25], some specific rules exist, so that, for a given transverse mode p, only a few in-plane modes participate with a non-vanishing contribution to the summation in Eq. (15). The rules are as follows:

- For a purely axisymmetric mode $\Phi_{(0,n)}$, only the axisymmetric in-plane modes $\{\Psi_{(0,i)}\}_{i\geq 1}$ participate to the summation.
- For an asymmetric mode $\Phi_{(k,n)}$ with $k\neq 0$, then the coupling involve only axisymmetric in-plane modes $\{\Psi_{(0,i)}\}_{i\geq 1}$ as well as asymmetric in-plane modes having twice the number of nodal diameters $\{\Psi_{(2k,i)}\}_{i\geq 1}$.

Hence for a given mode p, the convergence of the summation for $\Gamma^p_{p,p,p}$ is achieved within a small subset of all the possible in-plane modes. Let us denote by N_Ψ^{conv} the cardinal of this subset of admissible modes. The convergence of three coefficients $\Gamma^p_{p,p,p}$ is shown in Fig. 3, for three different modes of high frequencies. As simulations with a thousand modes are in view, the convergence of high-frequency modes has been selected for illustration. An axisymmetric mode with a large number of nodal circle, mode (0,18) has been selected together with a purely asymmetric one, mode (50,0), and a mixed mode : (24,8). Table 1 recalls the values of the first three modes and shows the order of appearance of the selected ones for illustration (nondimensional numbers are given for all numerical values). For asymmetric modes (k,n) with $k\neq 0$, the label p takes into account the two preferential configurations.

Fig. 3 reveals that, within the subset of admissible in-plane modes, the convergence is rather fast so that a number of 60 in-plane modes is enough to ensure the good convergence of all nonlinear coupling coefficients up to the 1000th transverse mode. For the purely axisymmetric modes, a simple rule of thumb is applicable, since the convergence is always obtained as soon as in-plane modes with twice the number of nodal circles than the selected transverse mode are taken into account. For asymmetric modes no such simple rule seems to exist. Note that for purely asymmetric modes such as the (50,0) used as

an example, the convergence is faster at the beginning but then very slow so that it appears difficult to achieve a four digits accuracy. However, for the given example, mode (50,0), a three-digits accuracy is obtained with $N_\Psi^{\text{conv}} = 33$ only, in line with the results for the other coefficients. For the remainder of the study, a computation with 1000 transverse and 60 in-plane modes has been realized and stored for all the subsequent calculations. This computation, made offline, is lengthy but valid for all circular plates.

3.2.3. Results of simulations

Two different cases are tested to show the versatility of the method. First the sound of a large gong (or Chinese tam-tam), with a bright, shimmering sound together with an audible cascade resulting in a build-up of energy to higher frequencies a few milliseconds after the strike is looked for. Second, the case of a strongly impacted thin crash cymbal, with a very large amount of energy to very high frequencies from the strike and a pronounced decay of energy is investigated. The parameters for these two cases are very different but both show a strongly nonlinear regime, giving a proof of the ability and flexibility of the numerical scheme to produce an extremely rich variety of realistic sounds.

The case of a large gong is obtained with the following parameters : radius $a=0.4$ m, thickness $h=1$ mm. The material parameters are selected (for all cases) as: $E=2.10^{11}$ Pa, $\nu=0.3$ and $\rho=7860$ kg m^{-3}. The first eigenfrequency is 7.7 Hz and the 1000th is 5747 Hz. The stability condition (38) for the sampling frequency $f_S = 1/k$ reads $f_S > \pi f_{1000}$ as 1000 modes will be used in the simulations, hence $f_S > 18\,055$ Hz. For the first set of simulations, the sampling frequency has been selected as 40 kHz. The input point where the strike excites the plate is located near the edge at $r = 0.92a$ and with an angle of $\pi/4$. For the output of the simulation, the displacement at $r = 0.896a$ is selected, with an angle of 0.519 rad in order to avoid a radius with too many modes having a nodal point.

The damping law is given mode by mode and can be chosen as desired. The generic term for mode p is of the form $c_p\dot{q}_p$. For the present case, the damping law is selected to follow a power-law: $c_p = 0.005\omega_p^{0.6}$ in dimensional form. This power-law has been selected as being representative of the damping in large metallic plates as measured in [31] and is used here to show how a complex frequency dependence can be easily used in the context of modal representation. Finally to simulate the impact of a soft mallet, the interaction time T_{wid} is selected as 6 ms. Fig. 4 shows the displacement of the output w and the spectrograms of the velocity, for two different amplitudes of the striking force: $p_m=40$ N and $p_m=80$ N. One can first remark that the amplitude of the displacement is larger than the thickness at the edge, with a maximum amplitude at $5h$ for the strike at 40 N and $7h$ for 80 N. An obvious build-up of energy, signature of the cascade, is observed for the two cases. While the spectrum of the input force contains frequencies up to around 1000 Hz, energy flows to the higher frequencies, up to 2500 Hz for the first strike, and 5000 Hz for the second. This property allows us to illustrate the optimal choice of the number of transverse modes N_Φ, which should be chosen as the maximal frequency present in the simulations. For the first case, one could have chosen to restrain the truncation to 500 modes as $f_{500}=2840$ Hz, in order to speed up the calculations. The choice of 1000 modes is large for the first case but optimal for the second case where the energy flows near the highest frequency available. One can also observe that the slope of the build-up of energies through frequencies increases with the amplitude of the strike. As demonstrated in [32], when damping is not present the increase of energy in the cascade should behave as $t^{1/3}$. Here the power-law behavior is slightly discernable but mostly hidden by the damping, as discussed for

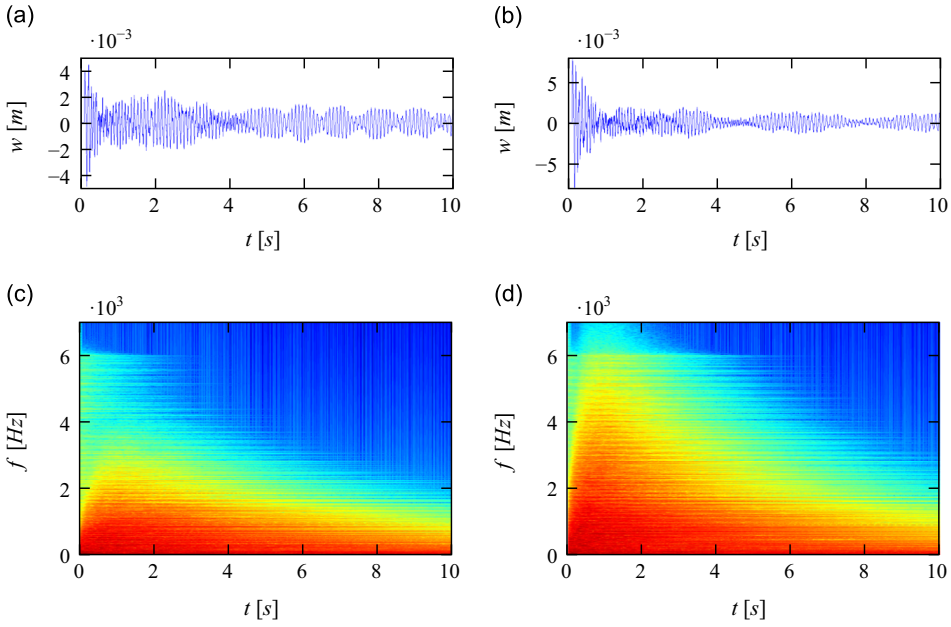

Fig. 4. Numerical simulation for the sound synthesis of a gong, $f_S=40$ kHz. Circular plate of radius $a=0.4$ m and thickness $h=1$ mm. (a), (c) Displacement and (b), (d) spectrograms of the output point w located at $r = 0.896a$. Soft strike with $T_{wid}=6$ ms and (a), (b) $p_m=40$ N, (c), (d) 80 N.

example in [31,32]. The sounds are given as supplementary material in the companion web-page of the paper.[1] They have been obtained from the velocity of the output point. One can remark that they are very realistic with an excellent timber richness.

The simulation times for these cases are indicatory given. The simulations are run on a standard desktop with single processor with a CPU clock at 2.4 GHz. The time needed for one seconds of sound is about 3 h at 40 kHz. Note that with respect to the stability condition, the sampling frequency f_S can be set to 20 kHz, resulting in a simulation time of 1h30 per second, without losing any quality in the sound produced. Finally, one could obtain better simulation times for the first case by selecting $N_\Phi = 500$, resulting in a simulation time of 35 min per second. By parallelizing the code or using better machine performance as e.g. GPU, there is no doubt that the proposed method allows one to obtain rich and realistic sounds for a reasonable computational cost.

The case of a crash cymbal is now investigated. The idea is to use the same framework and set the parameters so as to obtain the crashing sound of a small cymbal vigorously beaten by a woodstick. The radius is selected as $a=0.2$ m and the thickness as $h=0.5$ mm. With the material parameters unchanged, the first eigenfrequency is 15.5 Hz while the 1000th is 11 495 Hz. The minimum sampling frequency for ensuring stability is 36 100 Hz; it has thus been selected as 80 kHz in the simulations shown below. The strike parameters have been set to a small interaction time, thus $T_{wid}=1$ ms so as to excite a large bandwidth from the input, together with a larger amplitude p_m. The damping has been adjusted to larger values as compared to the gongs, and the law $c_p = 0.007\omega_p^{0.7}$ has been selected. The result of a simulation with a strike of amplitude $p_m=120$ N is shown in Fig. 5. During the first milliseconds after the strike, the vibration amplitude reaches 1 cm, 20 times the thickness. This results in a very quick build-up of energy with very high frequencies up to 20 kHz, which are evidenced in the zoom on the time domain together with the spectrogram. This case is thus very different from the previous one, where 1000 modes were enough to represent the frequency content of the strongly nonlinear regime. Here with 1000 modes the model contains modal components up to 11 500 Hz and the modal truncation is clearly seen in the spectrogram. However for sound synthesis purposes, the brilliance of the sound is very well represented with the modes up to 11 500 Hz, so that the truncation has no dramatic influence on the sound produced. Indeed, once again the sounds obtained are very realistic with a very rich spectrum and a particular brilliance, typical of a crashing sound.

3.3. A rectangular, simply-supported plate

3.3.1. Geometry and boundary conditions

In this section a rectangular plate with transverse simply-supported boundary conditions is chosen. The plate, with boundary δS, is supposed to have lateral dimension L_x, L_y. For the in-plane directions, a distinction is made in the literature between a movable and an immovable edge (see, for example, [33,2]). For the present work, a movable edge is selected, for which the conditions read (the subscripts $_n$, $_t$ refer, respectively, to the normal and tangent directions to δS)

$$w = 0 \quad \forall \mathbf{x} \in \delta S \tag{42a}$$

$$w_{,nn} + \nu w_{,tt} = 0 \quad \forall \mathbf{x} \in \delta S \tag{42b}$$

$$F_{,nt} = F_{,tt} = 0 \quad \forall \mathbf{x} \in \delta S \tag{42c}$$

Such conditions, despite not describing a load-free edge (a desirable case for sound synthesis), have the advantage of being particularly simple. The solution for the transverse modes, in fact, is given in terms of sine functions [21]

$$\Phi_k(\mathbf{x}) = \sin\frac{k_1\pi x}{L_x}\sin\frac{k_2\pi y}{L_y} \quad \text{for integers } k_1,\ k_2. \tag{43}$$

The eigenfrequencies are then easily obtained as

$$\omega_k^2 = \frac{D}{\rho h}\left[\left(\frac{k_1\pi}{L_x}\right)^2 + \left(\frac{k_2\pi}{L_y}\right)^2\right]^2. \tag{44}$$

The conditions for the in-plane function, on the other hand, can be worked out to yield a simplified form. Consider in fact the following conditions:

$$F = F_{,n} = 0 \quad \forall \mathbf{x} \in \delta S;$$

it is clear that these conditions are sufficient (but not necessary) to satisfy (42c) [17]. Such conditions, along with Eq. (5), reduce the quest for the eigenmodes Ψ_k to the clamped plate problem. Despite not having a closed-form solution, this problem was recently shown to have a semi-analytical solution based on the Rayleigh–Ritz method, yielding a few hundred eigenmodes and associated frequencies with precision to, at least, four significant digits [27]. In short, such method allows one to transform the continuous eigenvalue problem (Eq. (5)) to a discrete eigenvalue problem, easily treated by any eigenvalue routines in many programming languages (C, Matlab, etc.). For that, a generic eigenfunction Ψ_k is written as a

[1] The sounds for all the cases presented are given as wave files in the companion web-page of the paper hosted by Elsevier as well as in the following URL: http://www.ensta-paristech.fr/~touze/modalsynthesis.html. The reader is invited to listen to them for a perceptual comparison.

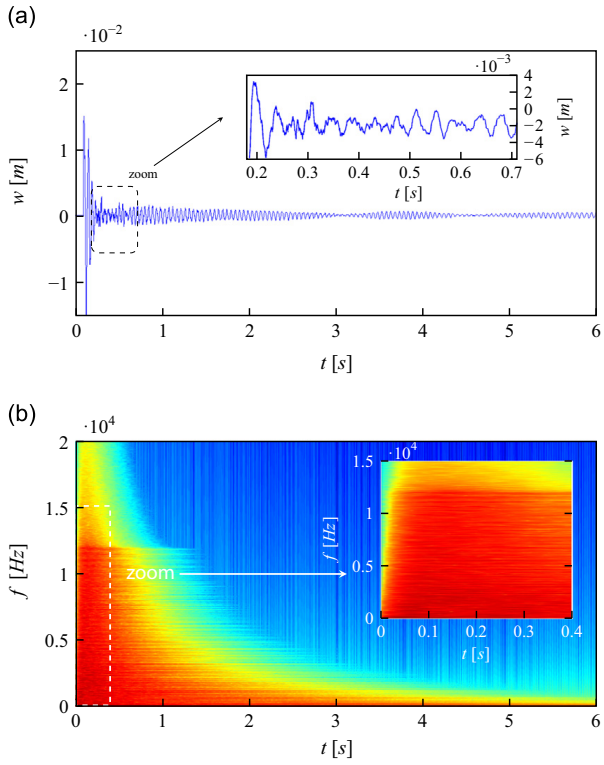

Fig. 5. Numerical simulation for the sound synthesis of a cymbal, $f_S=80$ kHz. Circular plate of radius $a=0.2$ m and thickness $h=0.5$ mm, hard impact with $T_{wid}=1$ ms and amplitude $p_m=120$ N. (a) Time series of displacement at $r=0.896a$, with a close-up to observe the high frequencies in the first milliseconds. (b) Spectrogram of the velocity at output point.

weighted sum of expansion functions, in the following way:

$$\Psi_k(\mathbf{x}) = \sum_{n=1}^{N_\Lambda} a_n \Lambda_n(\mathbf{x}), \tag{45}$$

for some carefully chosen functions Λ_n and unknown weights a_n. These weights, along with the eigenvalues ζ_k^4, are given by solving the eigenproblem

$$\mathbf{Ka} = \zeta^4 \mathbf{Ma}, \tag{46}$$

where $\mathbf{K}$, $\mathbf{M}$ are $N_\Lambda \times N_\Lambda$ matrices, obtained following the procedure detailed in [27]. The form of these matrices is given in Appendix C. Note that, as pointed out in Section 3.2.1, the weights and frequencies *depend* on the aspect-ratio of the plate, but they are invariant (up to a multiplying constant) for plates sharing the same aspect ratio.

3.3.2. Coupling coefficients

In this section, the convergence for some coupling coefficients is shown, and coupling rules given. The plate considered in this section has an aspect ratio $L_x/L_y = 2/3$. Note that nondimensional coefficients are obtained by multiplying $\Gamma^s_{k,m,n}$ as in Eq. (15) by $(L_xL_y)^3$ (these are the values plotted in the figures and considered in the table of this section).

As opposed to the circular case, it is difficult to have an a priori knowledge on the coupling rules. This is because the form of the in-plane eigenfunctions is not known analytically, and thus only a numerical investigation can help in laying out coupling rules. As for the circular case, coefficients of the kind $\Gamma^p_{p,p,p}$ are investigated. For $p \lesssim 50$, the coefficients converge quite rapidly with a number of in-plane modes $N_\Psi \sim 50$. Fig. 6 and Table 2 detail the convergence for some selected (k_1, k_2) modes, (k_1, k_2) being defined in Eq. (44). A "staircase"-like behavior, where the value seems to be converging before stepping in a discontinuous way to a higher value, is observed, as a reflection of the fact that numerous in-plane modes do not participate to the convergence of the $\Gamma^p_{p,p,p}$ coefficient. Hence, in order to obtain convergence, all in-plane modes must be retained. The convergence is found to be rapid when at least one between k_1 and k_2 is small. On the other hand, when both k_1 and k_2 are large, Fig. 6 shows that about 400 in-plane modes are necessary for the convergence of the $\sim$500th transverse mode. Note that the numerical method for the clamped case, detailed in Appendix B.2, was shown to yield robust solutions up to the 400–500th mode, so that convergence of high-range nonlinear coefficients becomes only approximate when considering a set of $\sim$1000 modes. Nonetheless, sound synthesis is still possible with the stable scheme and approximate nonlinear couplings.

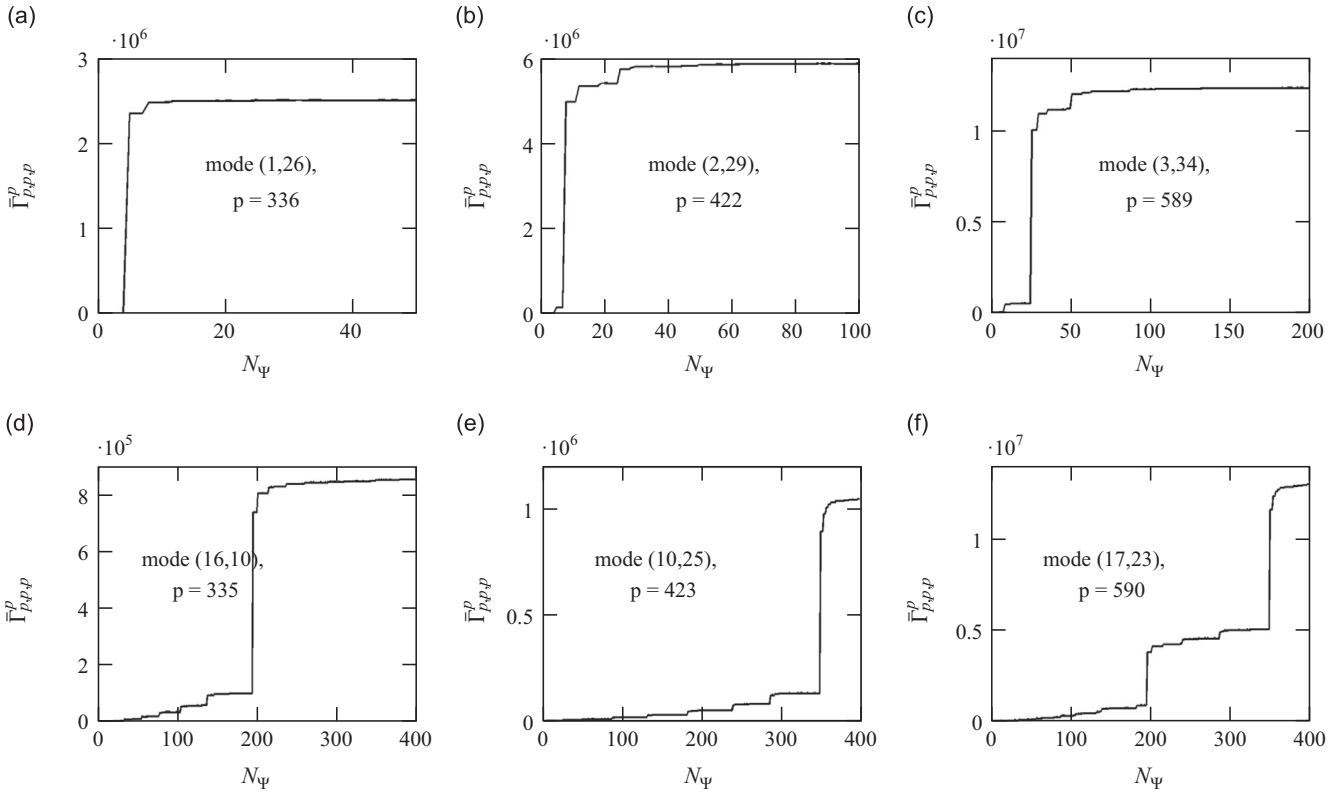

Fig. 6. Plots of a few nondimensional values of coupling coefficients, $\bar{\Gamma}^p_{p,p,p} = \Gamma^p_{p,p,p}(L_xL_y)^3$ for some modes of the rectangular plate with simply-supported edges. (a)–(c) High-order modes with a small modal index k_1, showing convergence. (d)–(f) High-order modes (adjacent to top ones) with large modal indices k_1, k_2.

Table 2
Nondimensional values of radian eigenfrequencies ω_k and coupling coefficients $\Gamma^p_{p,p,p}(L_xL_y)^3$ for some modes of the rectangular plate with simply-supported edges. The modes are sorted with respect to increasing eigenfrequencies. N_Ψ gives the number of modes needed to get the displayed (converged) value for the coupling coefficients (up to three significant figures). The indices k_1, k_2 are as in Eq. (44).

Mode label p	Mode (k_1, k_2)	ω_k	ω_k/ω_1	$\Gamma^p_{p,p,p}(L_xL_y)^3$	N_Ψ
1	(1,1)	89.101	1	2.00×10^1	12
20	(3,5)	1240.6	13.9	9.50×10^3	286
72	(5,10)	4283.7	48.1	1.07×10^5	239
336	(1,26)	18 595	208.7	2.50×10^6	25
422	(2,29)	23 303	261.5	5.88×10^6	103
589	(3,34)	32 248	361.9	1.23×10^7	132

3.3.3. Simulation results

In this section simulation results from a plate of aspect ratio $L_x/L_y = 2/3$ are presented. To simulate a steel plate, the physical parameters are chosen as $E = 2 \times 10^{11}$ Pa, $\rho = 7860$ kg/m^3, $\nu = 0.3$. The geometrical parameters are chosen as $L_x = 0.4$ m, $L_y = 0.6$ m, $h = 1.2$ mm. To discuss the effects of damping, two simulations are presented in Fig. 7. For both simulations, the idea is to strike the plate at high amplitudes in order to maximize the nonlinear effects. For that, the forcing parameters are chosen as $T_{wid} = 7$ ms, $p_m = 300$ N. The input is located at $[0.31L_x\ 0.43L_y]$, and the output is recorded at $[0.52L_x\ 0.37L_y]$. For figures (a)–(b), the damping law is selected as $c = 0.004\omega^{0.75} + 0.08$ kg/m^2/s. As opposed to the circular case, this damping law presents an added constant which dissipates energy at equal rates at all scales. This choice can be useful in order to dissipate the lowest frequencies in a reasonable time, so to avoid a low-frequency modulation (especially at the end of the time series) which may result unpleasant to the ear. For figures (c)–(d), all the parameters are kept unchanged except for the damping, which now reads $c = 0.04\omega^{0.75} + 0.08$ kg/m^2/s. Cases (a)–(b) simulate a hard contact (such as that of a wooden drumstick) which gives rise to a cascade of energy up to about 9000 Hz, and after which the damping effects start to dominate leaving a long queue typical of a gong. For this simulation, the number of retained modes is $N_\Phi = 500$, for which the highest eigenfrequency is 8034.6 Hz. The limiting sampling rate for stability according to Eq. (38) is 25 241 Hz, and for the current simulation the sampling rate is chosen as $f_S = 50\,482$ Hz. The time series (a) reveals that the amplitude of vibrations after the strike reaches almost 6 times the thickness, corresponding to a rich sound including pitch-glides and crashes. Comparing with figures (c)–(d), it is seen that the amplitude of vibrations remains unchanged. However, because of the increased loss effects, the cascade reaches its peak at about 4500 Hz. A comparison between the time series

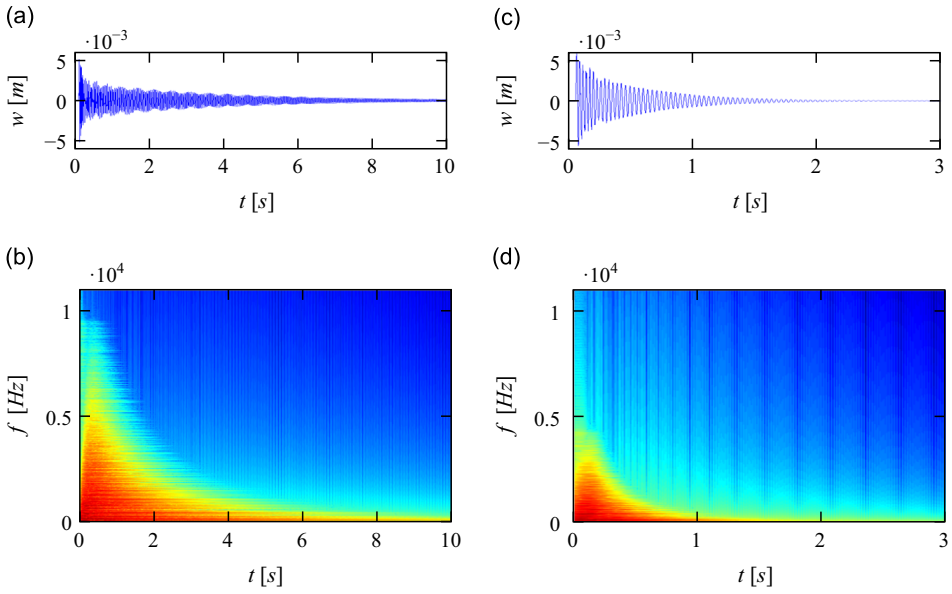

Fig. 7. Numerical simulations of a rectangular plate with L_x=0.4 m, L_y=0.6 m, h=1.2 mm. Time series of displacement at output point, spectrograms of velocity at output point, for T_{wid} = 7 ms, p_m=300 N. Damping law: $c = 0.04\omega^{0.75} + 0.08$ kg/m^2/s. (a), (b) $N_\Phi = 500$, $N_\Psi = 60$, f_S=50 482 Hz. (c), (d) $N_\Phi = 250$, $N_\Psi = 150$, f_S=25 624 Hz.

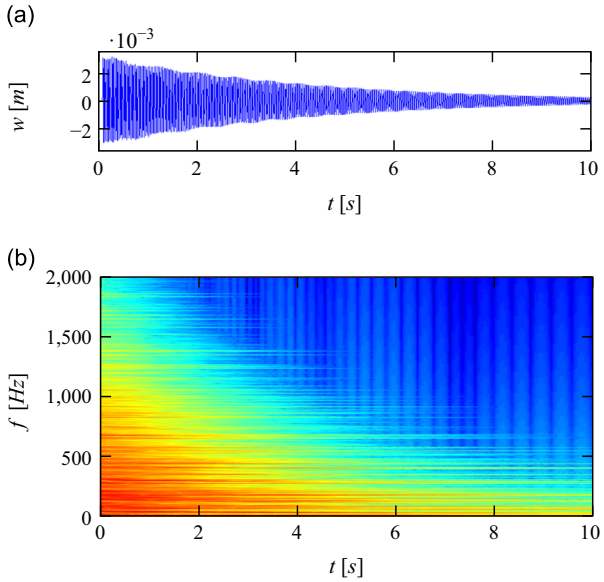

Fig. 8. Numerical simulation of a rectangular plate with L_x=0.4 m, L_y=0.6 m, h=1.2 mm, soft strike. (a) Time series of displacement at output point, (b) spectrograms of velocity at output point. T_{wid} = 8 ms, p_m=80 N, $N_\Phi = 100$, $N_\Psi = 150$, f_S=40 kHz, $c = 0.004\omega^{0.75} + 0.08$ kg/m^2/s.

(a) and (c) reveals that the high frequency modulations are dissipated almost instantly for the high-loss case, leaving only a few frequencies in the queue. However, because of the nonlinear effects at the start of the simulation, the sound remains rich: such a set of parameters may be used to simulate the sound of a gong held firmly at one point by the player. Very natural pitch-glides effects are prominent in this case. Because of the reduced number of eigenmodes activated, a sensible choice for this simulation is $N_\Phi = 250$, giving a largest eigenfrequency at 4078.3 Hz. The sampling rate is chosen again at twice as much the limiting frequency for stability, f_S=25 624 Hz. Indicative simulation times may be given as 28 min per second for (a)–(b) and 4 min per second for (c)–(d), in a fully optimized modal code in Matlab.

Another case of interest is depicted in Fig. 8, showing the case of a soft strike on the plate, and giving rise to a small cascade of energy with perceptually interesting loss effects. The plate is now hit using $T_{wid} = 8$ ms, p_m=80 N, and the damping law is again of the form $c = 0.004\omega^{0.75} + 0.08$ kg/m^2/s. The time series (a) reveals that these parameters are sufficient to give rise to nonlinear effects, as the amplitude of vibrations attains 2–3 times the thickness. However, the cascade reaches its peak at about 1500 Hz, suggesting that only a small number of modes may be employed for the current simulation. In fact, $N_\Phi = 100$ for Fig. 8. The limiting sampling frequency for stability would be in this case $f_S^{\lim} = 10\,559$ Hz, but in order to resolve accurately all the modes the sampling rate was chosen at f_S=40 kHz. The interesting thing about this

simulation is that with such a small number of modes a relatively short calculation time is needed: this is (indicatively) 1 min per second in Matlab. This can be viewed as an advantage of the modal approach with respect to other numerical techniques, namely Finite Differences: for weakly nonlinear vibrations (as in the present case), a few number of modes may be retained so to achieve faster calculation times. Despite the small number of retained modes, the sound is still surprisingly rich, as one may appreciate by listening to the sound sample in the companion page.

4. Conclusion

A general strategy for time-integrating nonlinear equations of motions for perfect and imperfect plates based on the von Kármán model has been derived in this paper. It relies on a modal approach coupled with an ad hoc energy-conserving scheme. Simulations with up to a thousand modes interacting nonlinearly are possible, and the stability of the scheme is guaranteed by selecting an appropriate timestep defined by the highest eigenfrequency of the discretized system. The method is completely general and can be applied to a large number of cases where the nonlinear dynamics is dominating, and where accuracy is needed together with a reasonable computational burden. The main advantages of the method are the following:

- The linear and nonlinear parameters appearing in the modal equations can be calculated with any degree of accuracy during an offline calculation. For the cases where the modes are known analytically, the values of the linear coefficients are exact, while the convergence of the nonlinear coefficients is obtained within a reasonable computational time.
- The generality of the proposed method can be extended to more difficult cases where the modes are not known analytically: such consideration is quite remarkable considering the diffused misconception according to which modal methods are only applicable in the few cases where the modes present a closed-form solution. A first example of a rectangular plate where the in-plane modes are not analytic is treated here by the Rayleigh–Ritz method. Different techniques may be employed for different cases, for instance finite-element techniques for the calculation of the nonlinear coefficients, as shown in [30].
- The stability condition derived from the analysis of the energy-conserving scheme shows that the sampling frequency f_S needs to be larger than πf_{N_Φ}, where f_{N_Φ} refers to the largest eigenfrequency contained in the truncation, hence resulting in a large timestep enabling faster simulations.
- A salient feature of the modal approach is the possibility of selecting ad hoc viscous damping laws effortlessly. Such feature is neglected in a finite element or finite difference context, where a temporal evolution operator describing the damping law has to be made explicit and global. This feature is a great advantage of the present method, allowing one to take into account very complex damping mechanisms.

The modal framework has been used here for the sound synthesis of cymbals and gong-like instruments. This example was chosen because it is a challenging one, with a strongly nonlinear dynamics involving hundreds of modes interacting in a turbulent manner. Perceptual accuracy is achieved thanks to the refined loss model implemented in the current flexible scheme. The sound examples have shown the ability of the method to compute very realistic sounds. It has been also shown how the tuning of the truncation coefficient can be selected in order to speed up the computations without loss in accuracy.

The results presented in this contribution show undoubtedly that the modal method is able to treat the cases of strongly nonlinear systems, with a huge number of modes interacting together. The authors believe that this should give new impetus in favour of modal schemes for nonlinear systems: because of its specific advantages – like those highlighted in this paper – the modal approach offers an attractive alternative to other numerical schemes.

Acknowledgments

The authors want to thank Olivier Thomas for a long-lasting interest in nonlinear vibrations of thin plates and the modal approach. Antoine Chaigne is thanked for initiating the very first steps of this research ten years ago, David Raus for his help in the first versions of the circular plate programs, and finally Stefan Bilbao for a continuous interest in energy-conserving schemes.

Appendix A. Energy-conserving modal scheme for imperfect plates

This appendix is devoted to extend the conservative scheme in modal coordinates for the case of an imperfect plate. Let $w_0(\mathbf{x})$ be the static deflection of the imperfect plate at rest, and $w(\mathbf{x}, t)$ the transverse displacement with respect to the static position w_0, then the von Kármán equations for imperfect plates simply read [34,35]

$$\rho h\ddot{w} + D\Delta\Delta w = \mathcal{L}(w + w_0, F) + p(\mathbf{x}, t) - R(\mathbf{x}, t), \tag{A.1a}$$

$$\Delta\Delta F = -\frac{Eh}{2}\mathcal{L}(w, w + 2w_0), \tag{A.1b}$$

The presence of an imperfection introduces quadratic nonlinear terms in the equations of motion (A.1). An interesting strategy for solving out the PDEs without recalculating the eigenmodes for each possible imperfection $w_0(\mathbf{x})$ consists in using the eigenmodes of the perfect plate as functional basis [35]. Within this framework, the continuous energies are found to have the same expressions as those given in Eqs. (19).

The framework of Section 2.2 is adapted by projecting also the imperfection on the modes of the transverse motion as

$$w_0(\mathbf{x}) = S_w \sum_{k=1}^{N_\Phi} \frac{\Phi_k(\mathbf{x})}{\|\Phi_k\|} a_k. \tag{A.2}$$

Following the same lines of calculation as for the perfect plate, the modal equations are obtained in the quadratic (q,η) formulation as

$$\ddot{q}_s + \omega_s^2 q_s + 2\xi_s \omega_s \dot{q}_s = \frac{S_F}{\rho h} \sum_{k=1}^{N_\Phi} \sum_{l=1}^{N_\Psi} E^s_{k,l}(q_k + a_k)\eta_l + p_s(t), \tag{A.3a}$$

$$\eta_l = -\frac{Eh}{2\zeta_l^4} \frac{S_w^2}{S_F} \sum_{m,n}^{N_\Phi} H^l_{m,n}(q_m q_n + 2q_m a_n). \tag{A.3b}$$

Using the property $E^s_{k,l} = H^l_{k,s}$, the associated conservative scheme is introduced for the undamped and unforced problem as

$$\delta_{tt} q_s(n) + \omega_s^2 q_s(n) = \frac{S_F}{\rho h} \sum_{k=1}^{N_\Phi} \sum_{l=1}^{N_\Psi} H^l_{k,s}(q_k(n) + a_k)\mu_{t\cdot}\eta_l(n), \tag{A.4a}$$

$$\mu_{t-}\eta_l(n) = -\frac{Eh}{2\zeta_l^4} \frac{S_w^2}{S_F} \sum_{i,j=1}^{N_\Phi} H^l_{i,j}\Big(q_i(n) e_{t-} q_j(n) + 2a_j\, \mu_{t-} q_i(n)\Big). \tag{A.4b}$$

The proof that such a scheme is energy conserving follows the lines of the previous demonstration. The second equation (A.4b) is multiplied by δ_{t+}. Using the symmetry property of the tensor $H^l_{i,j}$ together with the following identity on the discrete operators : $\delta_{t+}(\mu_{t-} q_i(n)) = \delta_{t\cdot} q_i(n)$, one obtains, similar to Eq. (29),

$$\sum_{k,s=1}^{N_\Phi} H^l_{k,s}(q_k(n) + a_k)\delta_{t\cdot} q_s(n) = -\frac{\zeta_l^4 S_F}{EhS_w^2} \mu_{t-}\left(\delta_{t+}\eta_l(n)\right) \tag{A.5}$$

Then, Eq. (A.4a) is multiplied by $\rho h \delta_{t\cdot} q_s(n)$ and then summed over the index s. Using (A.5), the same substitutions as in the previous case can be realized, leading to Eq. (32), from which the discrete energies can be identified as in Eqs. (33).

Appendix B. Mode shapes for the circular plate with free edge

B.1. Transverse modes Φ_p

The presentation of the results for the eigenproblem of a circular plate follows strictly reference [25]. Note that the results are given here, for the sake of generality, for the nondimensional problem. The eigenmodes Φ with a free boundary condition shall satisfy, for all θ and t:

$$(\Delta\Delta - \xi^4)\Phi = 0, \tag{B.1a}$$

$$\Phi_{,rr} + \nu\Phi_{,r} + \nu\Phi_{,\theta\theta} = 0 \quad \text{at } r = 1 \tag{B.1b}$$

$$\Phi_{,rrr} + \Phi_{,rr} - \Phi_{,r} + (2-\nu)\Phi_{,r\theta\theta} - (3-\nu)\Phi_{,\theta\theta} = 0 \quad \text{at } r = 1, \tag{B.1c}$$

$$\Phi(r=0) \quad \text{is bounded}, \tag{B.1d}$$

with $\xi^4 = \omega^2$. The solutions of the previous set are separated in r and θ, and write

$$\Phi_{0n}(r,\theta) = R_{0n}(r) \quad \text{for } k = 0 \tag{B.2a}$$

$$\begin{vmatrix} \Phi_{kn1}(r,\theta) \\ \Phi_{kn2}(r,\theta) \end{vmatrix} = R_{kn}(r) \begin{vmatrix} \cos k\theta \\ \sin k\theta \end{vmatrix} \quad \text{for } k > 0 \tag{B.2b}$$

with

$$R_{kn}(r) = \kappa_{kn}\left[J_k(\xi_{kn} r) - \frac{\widetilde{J}_k(\xi_{kn})}{\widetilde{I}_k(\xi_{kn})} I_k(\xi_{kn} r)\right] \tag{B.3}$$

where J_k is the Bessel functions of order k of the first kind, $I_k(x)=J_k(\mathrm{i}x)$ with $\mathrm{i}=\sqrt{-1}$, and $\widetilde{J}_k$ and $\widetilde{I}_k$ are defined as follows:

$$\widetilde{J}_k(x)=x^2J_{k-2}(x)+x(\nu-2k+1)J_{k-1}(x)+k(k+1)(1-\nu)J_k(x), \tag{B.4a}$$

$$\widetilde{I}_k(x)=x^2I_{k-2}(x)+x(\nu-2k+1)I_{k-1}(x)+k(k+1)(1-\nu)I_k(x). \tag{B.4b}$$

κ_{kn} is a normalization constant which can be chosen such that $\int_{(\mathcal{S})}\Phi_{kn}^2\,\mathrm{d}S=1$.

ξ_{kn} is the $\widetilde{n}$−th solution of the following equation:

$$\begin{aligned}&\widetilde{I}_k(\xi)\left[\xi^3J_{k-3}(\xi)+\xi^2(4-3k)J_{k-2}(\xi)+\xi k(k(1+\nu)-2)J_{k-1}(\xi)+k^2(1-\nu)(1+k)J_k(\xi)\right]\\&-\widetilde{J}_k(\xi)\left[\xi^3I_{k-3}(\xi)+\xi^2(4-3k)I_{k-2}(\xi)+\xi k(k(1+\nu)-2)I_{k-1}(\xi)+k^2(1-\nu)(1+k)I_k(\xi)\right]=0.\end{aligned} \tag{B.5}$$

k is found to be the number of nodal radii. Because of the free edge boundary condition, the edge of the plate is not a nodal circle, and mode Φ_{10} is a rigid body mode. So, the number n of nodal circles is not equal to $\widetilde{n}$. In fact, for $k=1$, $n=\widetilde{n}$ and for $k\neq 1$, $n=\widetilde{n}-1$ [25,36]. Numerical solutions for the zeros of Eq. (B.5) give the eigenfrequencies for the transverse problem since $\omega_{kn}=\xi_{kn}^2$.

B.2. In-plane modes Ψ_s

The boundary conditions for the plate with a free edge correspond to a free boundary for the in-plane displacements. Expressing these conditions in terms of the Airy stress function F leads to consider, due to the relationship between F and the in-plane displacements, a clamped edge condition [25,27]. The nondimensional eigenproblem to be solved for the in-plane modes Ψ thus reads, for all θ and t:

$$(\Delta\Delta-\zeta^4)\Psi=0, \tag{B.6a}$$

$$\Psi=0 \quad \text{at } r=1 \tag{B.6b}$$

$$\Psi_{,r}=0 \quad \text{at } r=1, \tag{B.6c}$$

$$\Psi(r=0) \quad \text{is finite.} \tag{B.6d}$$

The solutions of the previous set are separated in r and θ:

$$\Psi_{0m}(r,\theta)=S_{0m}(r) \quad \text{for } l=0 \tag{B.7a}$$

$$\left.\begin{matrix}\Psi_{lm1}(r,\theta)\\ \Psi_{lm2}(r,\theta)\end{matrix}\right|=S_{lm}(r)\left|\begin{matrix}\cos l\theta\\ \sin l\theta\end{matrix}\right. \quad \text{for} \quad l>0 \tag{B.7b}$$

with

$$S_{lm}(r)=\lambda_{lm}\left[J_l(\zeta_{lm}r)-\frac{J_l(\zeta_{lm})}{I_l(\zeta_{lm})}I_l(\zeta_{lm}r)\right] \tag{B.8}$$

where the ζ_{lm} is the m-th solution of the following equation:

$$J_{l-1}(\zeta)I_l(\zeta)-I_{l-1}(\zeta)J_l(\zeta)=0. \tag{B.9}$$

The normalization constant λ_{lm} is generally chosen so that $\int_{(\mathcal{S})}\Psi_{lm}^2\,\mathrm{d}S=1$. In this case, l,m correspond to the numbers of nodal radii and circles, respectively.

Appendix C. Modes for rectangular plate with clamped edges

The method described here for computing efficiently the eigenmodes of a rectangular plate with clamped edges has been derived first in [27,28], where it was shown to be a fast-converging, accurate and stable method up to the 400–500th mode. The problem is solved using the Rayleigh–Ritz method with appropriate expansion functions. For a generic mode $\Psi(\mathbf{x})$, consider then the following expansion:

$$\Psi(\mathbf{x})=\sum_{n=1}^{N_\Lambda}a_n\Lambda_n(\mathbf{x}).$$

The functions Λ_n are written as

$$\Lambda_n(\mathbf{x})=X_{n_1}(x)Y_{n_2}(y), \tag{C.1}$$

where

$$X_{n_1}(x) = \cos\left(\frac{n_1\pi x}{L_x}\right) + \frac{15(1+(-1)^{n_1})}{L_x^4}x^4 - \frac{4(8+7(-1)^{n_1})}{L_x^3}x^3 + \frac{6(3+2(-1)^{n_1})}{L_x^2}x^2 - 1, \tag{C.2}$$

and similarly for $Y_{n_2}(y)$

The algebraic eigenvalue problem is written as

$$\mathbf{Ka} = \zeta^4\mathbf{Ma}, \tag{C.3}$$

and gives the expansion weights **a** along with the eigenvalues ζ^4. The stiffness and mass matrices for the clamped plate problem are set up as follows (primes indicate derivatives):

$$K(i,j) = K(mn,pq)$$
$$= \int_0^{L_x} X''_m(x)X''_p(x)\,\mathrm{d}x \int_0^{L_y} Y_n(y)Y_q(y)\,\mathrm{d}y + \int_0^{L_x} X_m(x)X_p(x)\,\mathrm{d}x \int_0^{L_y} Y''_n(y)Y''_q(y)\,\mathrm{d}y + 2\int_0^{L_x} X'_m(x)X'_p(x)\,\mathrm{d}x \int_0^{L_y} Y'_n(y)Y'_q(y)\,\mathrm{d}y$$

$$M(i,j) = M(mn,pq) = \int_0^{L_x} X_m(x)X_p(x)\,\mathrm{d}x \int_0^{L_y} Y_n(y)Y_q(y)\,\mathrm{d}y$$

The integrals can be calculated analytically, and are

$$\int_0^{L_x} X''_m(x)X''_p(x)\,\mathrm{d}x = \begin{cases} 720/L_x^3 & \text{if } m=p=0 \\ (\pi^4m^4 - 672(-1)^m - 768)/(2L_x^3) & \text{if } m=p\neq 0 \\ 0 & \text{if } m \text{ or } p=0 \text{ and } m\neq p \\ -24(7(-1)^m + 7(-1)^p + 8(-1)^m(-1)^p + 8)/L_x^3 & \text{otherwise} \end{cases}$$

$$\int_0^{L_x} X_m(x)X_p(x)\,\mathrm{d}x = \begin{cases} 10L_x/7 & \text{if } m=p=0 \\ 67L_x/70 - (-1)^mL_x/35 - 768L_x/(\pi^4m^4) - 672(-1)^mL_x/(\pi^4m^4) & \text{if } m=p\neq 0 \\ 3L_x((-1)^p+1)(\pi^4p^4 - 1680))/(14\pi^4p^4) & \text{if } m=0 \text{ and } p\neq 0 \\ 3L_x((-1)^m+1)(\pi^4m^4 - 1680))/(14\pi^4m^4) & \text{if } p=0 \text{ and } m\neq 0 \\ -(L_x(11\,760(-1)^m + 11\,760(-1)^p - 16\pi^4m^4 + 13\,440(-1)^m(-1)^p + & \\ (-1)^m\pi^4m^4 + (-1)^p\pi^4m^4 - 16(-1)^m(-1)^p\pi^4m^4 + 13\,440))/(70\pi^4m^4) & \\ -(L_x(13\,440m^4 + 11\,760(-1)^mm^4 + 11\,760(-1)^pm^4 + 13\,440(-1)^m(-1)^pm^4))/(70\pi^4m^4p^4) & \text{otherwise} \end{cases}$$

$$\int_0^{L_x} X''_m(x)X_p(x)\,\mathrm{d}x = \begin{cases} -120/(7L) & \text{if } m=p=0 \\ -(768\pi^2m^2 - 47\,040(-1)^m + 35\pi^4m^4 + 432(-1)^m\pi^2m^2 - 53\,760)/(70L_x\pi^2m^2) & \text{if } m=p\neq 0 \\ -(60((-1)^p+1)(\pi^2p^2 - 42))/(7L_x\pi^2p^2) & \text{if } m=0 \text{ and } p\neq 0 \\ -(60((-1)^m+1)(\pi^2m^2 - 42))/(7L_x\pi^2m^2) & \text{if } p=0 \text{ and } m\neq 0 \\ (24(m^2+p^2)(7(-1)^m + 7(-1)^p + 8(-1)^m(-1)^p + 8))/(L_x\pi^2m^2p^2) & \\ -((108(-1)^m + 108(-1)^p + 192(-1)^m(-1)^p + 192))/(35L_x) & \text{otherwise} \end{cases}$$

and similarly for the integrals involving the functions Y.

Appendix D. Supplementary data

Supplementary data associated with this paper can be found in the online version at http://dx.doi.org/10.1016/j.jsv.2015.01.029.

References

[1] A.H. Nayfeh, *Nonlinear Interactions: Analytical, Computational and Experimental Methods*, *Wiley Series in Nonlinear Science*, Wiley, New York, 2000.
[2] M. Amabili, *Nonlinear Vibrations and Stability of Shells and Plates*, Cambridge University Press, Cambridge, 2008.
[3] C. Touze, S. Bilbao, O. Cadot, Transition scenario to turbulence in thin vibrating plates, *Journal of Sound and Vibration* 331 (2) (2012) 412–433.
[4] G. Düring, C. Josserand, S. Rica, Weak turbulence for a vibrating plate: *Can one hear a Kolmogorov spectrum? Physical Review Letters* 97 (2006) 025503.
[5] A. Boudaoud, O. Cadot, B. Odille, C. Touzé, Observation of wave turbulence in vibrating plates, *Physical Review Letters* 100 (2008) 234504.
[6] N. Mordant, Are there waves in elastic wave turbulence ? *Physical Review Letters* 100 (2008) 234505.
[7] P. Cobelli, P. Petitjeans, A. Maurel, V. Pagneux, N. Mordant, Space–time resolved wave turbulence in a vibrating plate, *Physical Review Letters* 103 (2009) 204301.
[8] N.H. Fletcher, T.D. Rossing, *The Physics of Musical Instruments*, second edition, Springer, New York, 1998.
[9] K. Legge, N.H. Fletcher, Nonlinearity, chaos, and the sound of shallow gongs, *Journal of the Acoustical Society of America* 86 (6) (1989) 2439–2443.
[10] A. Chaigne, C. Touzé, O. Thomas, Nonlinear vibrations and chaos in gongs and cymbals, *Acoustical Science and Technology, Acoustical Society of Japan* 26 (5) (2005) 403–409.
[11] S. Bilbao, *Numerical Sound Synthesis: Finite Difference Schemes and Simulation in Musical Acoustics*, Wiley, Chichester, 2009.

[12] S. Bilbao, Percussion synthesis based on models of nonlinear shell vibration, *IEEE Transactions on Audio, Speech and Language Processing* 18 (4) (2010) 872–880.
[13] J. Chadwick, S. An, D. James, Harmonic shells: a practical nonlinear sound model for near-rigid thin shells, *ACM Transactions on Graphics* (*SIGGRAPH ASIA Conference Proceedings*) 28 (5) (2009) Article 119.
[14] T. von Kármán, Festigkeitsprobleme im maschinenbau, *Encyklop die der Mathematischen Wissenschaften* 4 (4) (1910) 311–385.
[15] A.H. Nayfeh, D.T. Mook, *Nonlinear Oscillations*, John Wiley & Sons, New York, 1979.
[16] C. Chia, *Nonlinear Analysis of Plates*, McGraw Hill, New York, 1980.
[17] O. Thomas, S. Bilbao, Geometrically nonlinear flexural vibrations of plates: *in-plane boundary conditions and some symmetry properties*, *Journal of Sound and Vibration* 315 (3) (2008) 569–590.
[18] L. Landau, E. Lifschitz, *Theory of Elasticity*, third edition, Elsevier Butterworth Heinemann, Oxford, 1986.
[19] A.H. Nayfeh, P.F. Pai, *Linear and Nonlinear Structural Mechanics*, Wiley, New York, 2004.
[20] P. Ciarlet, L. Gratie, From the classical to generalized von Kármán and Marguerre–von Kármán equations, *Journal of Computational and Applied Mathematics* 190 (2006) 470–486.
[21] P. Hagedorn, A. DasGupta, *Vibrations and Waves in Continuous Mechanical Systems*, Wiley, New York, 2007.
[22] A. Chaigne, C. Lambourg, Time-domain simulation of damped impacted plates. i. Theory and experiments, *The Journal of the Acoustical Society of America* 109 (4) (2001) 1422–1432.
[23] C. Lambourg, A. Chaigne, D. Matignon, Time-domain simulation of damped impacted plates. II. Numerical model and results, *Journal of the Acoustical Society of America* 109 (4) (2001) 1433–1447.
[24] S. Sridhar, D.T. Mook, A.H. Nayfeh, Non-linear resonances in the forced responses of plates, part I: *symmetric responses of circular plates*, *Journal of Sound and Vibration* 41 (3) (1975) 359–373.
[25] C. Touzé, O. Thomas, A. Chaigne, Asymmetric non-linear forced vibrations of free-edge circular plates, part I: *theory*, *Journal of Sound and Vibration* 258 (4) (2002) 649–676.
[26] C. Touzé, O. Thomas, Non-linear behaviour of free-edge shallow spherical shells: effect of the geometry, *International Journal of Non-linear Mechanics* 41 (5) (2006) 678–692.
[27] M. Ducceschi, C. Touzé, S. Bilbao, C. Webb, Nonlinear dynamics of rectangular plates: *investigation of modal interaction in free and forced vibrations*, *Acta Mechanica* 225 (1) (2014) 213–232.
[28] M. Ducceschi, Nonlinear Vibrations of Thin Rectangular Plates. A Numerical Investigation with Application to Wave Turbulence and Sound Synthesis, PhD Thesis, ENSTA-ParisTech, 2014.
[29] S. Bilbao, A family of conservative finite difference schemes for the dynamical von Kármán plate equations, *Numerical Methods for Partial Differential Equations* 24 (1) (2007) 193–216.
[30] C. Touzé, M. Vidrascu, D. Chapelle, Direct finite element computation of non-linear modal coupling coefficients for reduced-order shell models, *Computational Mechanics* 54 (2) (2014) 567–580.
[31] T. Humbert, O. Cadot, G. Düring, S. Rica, C. Touzé, Wave turbulence in vibrating plates: *the effect of damping*, *Europhysics Letters* 102 (3) (2013) 30002.
[32] M. Ducceschi, O. Cadot, C. Touzé, S. Bilbao, Dynamics of the wave turbulence spectrum in vibrating plates: *a numerical investigation using a conservative finite difference scheme*, *Physica D* 280–281 (2014) 73–85.
[33] M. Amabili, Nonlinear vibrations of rectangular plates with different boundary conditions: *theory and experiments*, *Computers and Structures* 82 (2004) 2587–2605.
[34] G. Ostiguy, S. Sassi, Effects of initial imperfections on dynamic behaviour of rectangular plates, *Non-linear Dynamics* 3 (1992) 165–181.
[35] C. Camier, C. Touzé, O. Thomas, Non-linear vibrations of imperfect free-edge circular plates and shells, *European Journal of Mechanics A/Solids* 28 (2009) 500–515.
[36] A.W. Leissa, *Vibration of Plates*, Acoustical Society of America, New York, 1993 (orig. issued NASA SP-160, 1969).